Available online at www.sciencedirect.com

ScienceDirect

Ceramics International 40 (2014) 1667–1674

CERAMICS INTERNATIONAL

www.elsevier.com/locate/ceramint

Porosity formation and enhanced solubility of calcium silicate hydrate in hydrothermal synthesis

Wei Guan, Fangying Ji*, Dexin Fang, Yong Cheng, Zhuoyao Fang, Qingkong Chen, Peng Yan

Key Laboratory of Three Gorges Reservoir Region's Eco-Environment, Ministry of Education, Chongqing University, Chongqing 400045, PR China

Received 7 July 2013; received in revised form 11 July 2013; accepted 11 July 2013
Available online 20 July 2013

Abstract

The objective of this paper was to determine the optimal stirring speed for hydrothermal synthesis of calcium silicate hydrate (CSH) with porous structures. Using Field-emission Scanning Electron Microscopy (FESEM), Brunauer–Emmett–Teller (BET), X-ray diffraction (XRD), and Particle size distributions (PSD), coupled with the Improved of Detached Eddy Simulation (IDDES), porous structure formation mechanisms at different stirring speeds were examined. The CSH formation process was a step-by-step pattern during a complex phase condition; however, CSH with porous structure could be obtained effectively under reasonable stirring speed. The established Avrami Dissolution Dynamics Model indicated that the as-prepared CSH exhibited greatly enhanced Ca^{2+} and OH^- release under proper stirring speed. This was likely due to small particle size, low crystallinity, and large specific surface area (S_{BET}). This porous CSH has potential application in phosphorus removal from wastewater via production of HAP, thus reducing the negative environmental effects of continual natural phosphorus resource depletion.

Keywords: B. Porosity; D. SiO_2; E. Functional applications; Chemical preparations

1. Introduction

Calcium silicate hydrate (CSH) is widely used in the removal and recycling of mineral nutrients found in wastewater [1–5]. For example, phosphorus (P), as a non-renewable and essential nutrient is rapidly being exhausted through its use in various industries [6–11]. The spontaneous release of Ca^{2+} and OH^- from CSH allows for rapid production of hydroxyapatite ($Ca_5(PO_4)_3(OH)$) making it an effective means for P recovery [5,12]. However, the effectiveness of its use may benefit from enhancement of CSH solubility.

According to the dissolution kinetics of inorganic solids, a large specific surface area (S_{BET}) is beneficial to enhancement of the solubility [13–15]. In addition, several studies have demonstrated the effectiveness of hydrothermal synthesis in synthesizing and developing porous materials with large S_{BET} [16–19]. This is due in large part to the unique properties of water found within the hydrothermal system, (e.g. temperature effects on vapor pressure, increased ion concentrations, changes in density etc.). These same properties allow for the easier formation of intermediate and metastable states, and other special phase under hydrothermal conditions.

The CSH materials, (e.g. Tobermorite, Xonotlite, etc.) presently used to recover P are prepared via this hydrothermal synthesis process [20–22]. Unfortunately, and primarily due to poor solubility of these materials their use in P recovery is somewhat limited [12,23]. It has been reported that improving the Ca/Si mole ratio can increase the content of calcium in CSH [2]. However, doing so does not alone enhance the release of Ca^{2+} and OH^-. This is due in large part to the complexity of CSH formation, a complicated, inhomogeneous, and multiphase chemical reaction. This reaction involves the transition from a combined solid–liquid–gas phase to a single gel phase [24,25]. Thus, during a hydrothermal reaction, the viscosity of the reaction slurry is in constant flux. Understanding the formation mechanism for CSH is therefore relatively difficult to achieve via experiments alone, as are the formation of porous structures, and the mechanism(s) involved in enhancement of solubility.

*Corresponding author. Tel./fax: +86 23 65127537.
E-mail address: jfytougao@163.com (F. Ji).

0272-8842/$ - see front matter © 2013 Elsevier Ltd and Techna Group S.r.l. All rights reserved.
http://dx.doi.org/10.1016/j.ceramint.2013.07.058

Therefore, in an attempt to provide some insight into these complex processes, this study investigated the influence of stirring intensity on the porous structure, and solubility of CSH. Porous CSH was prepared via dynamic hydrothermal synthesis, with calcium oxide and silicon dioxide as the raw materials. Several important characteristics of CSH (e.g. S_{BET}, crystallinity, and particle size distribution) change significantly as stirring intensity changes. According to the Avrami Dissolution Kinetic Theory, these characteristics all have significant influence on solubility. Based on Ansys14.0, the Improved Delayed Eddy Simulation (IDDES) was used as the turbulence model of fluid flow and adopted to fit local complex flow area. Doing so allowed for the systematic evaluation of CSH porous structure formation mechanism(s) under complex phase states. This as-prepared porous CSH was relatively more soluble, suggesting its enhanced effectiveness in P recovery processes.

2. Experimental procedure

2.1. Raw materials

The CaO material (carbide residue, CaO > 75%), and SiO_2 material (Silica, SiO_2 > 97%) used for CSH synthesis was originally derived from industrial waste, and provided directly by the Chongqing Changshou Chemical Co. Ltd., and stored in sealed bottles until use. The chemical composition of the carbide residue and silica are presented in Table 1.

2.2. Hydrothermal synthesis experiments of porous CSH

In a typical experiment, 300 ml CSH slurry was prepared using silica to carbide residue liquid/solid ratio of 30/1, and a Ca/Si molar ratio of 1.75/1. The resulting slurry was poured into high-pressure kettles (2.4 MPa) at 170 °C, and stirred at 30, 50, 70, 90 and 110 rpm for 6 h, respectively. Slurries were then removed and dried for 2h at 105 °C. All samples were labeled according to respective stirring conditions as follows: CSH (30 rpm), CSH (50 rpm), CSH (70 rpm), CSH (90 rpm), and lastly CSH (110 rpm).

2.3. Physical modeling of the high-pressure reaction kettle

2.3.1. Establishment of the three-dimensional (3D) entity model

The component model of the reactor stirring paddle was established using the GAMBIT model software [26,27]. Using the 3D curved surface processing function, and the special fitting function within GAMBIT, the actual 3D coordinates were translated to the local characteristic curves to create the 3D entity model. The ratio of actual size between the physical model, and the reactor stirring paddle component was 1:1. The direction of impeller rotation was determined by the right-hand screw rule. And as shown in Fig. 1, rotation was in a clockwise direction.

2.3.2. The computational domain layout and GAMBIT-mesh

The flow field calculation areas of the reactor were divided into two main parts, (1) the rotating fluid region near the reactor stirring paddle component, and (2) any remaining regions. The cylindrical reactor was 60 mm in diameter, and 200 mm in height (Fig. 2).

The flow field around the center of stirring paddle was relatively complex. The local pressure and velocity gradient around this area were extremely large. This was especially true for the flow parameters within the inner adhering layer of the stirring paddle boundary layer. In addition, the adhering grid at the paddle surface, created by non-structured grid, had poor resolution on the flow information of adhering surface. Therefore, the sliding grid processing technology was adopted to efficiently transfer information between the fluid flow regions located near the agitating reactor components, and the regions inside the cylinder. The hybrid grid theory, coupled wall function of leaf blade near wall zone, was introduced in order to capture more information about flow within the local complex flow field. The total number of computational domain grids was more than 600,000. The layout of these computational domain grids is presented in Fig. 3.

2.3.3. Calculation of flow fields

Using the fluent calculation module within Ansys 14.0 to calculate fluid dynamics, an IDDES model was adopted as the turbulence model for use in flow field calculations. In this method, the DDES and WMLES were combined to express identical expression formula by modifying the subgrid scale model length, and by the association function. This allowed for the solving of the discrete logarithmic layer problem, thereby enhancing the accuracy of flow field calculations under the complex stress conditions. The reaction kettle was assumed as the stationary boundary wall. The reactor impeller components wall was considered as the boundary of the rotating wall. The rotating wall rotated around the X axis at 90 rpm in the reference of the rotating area defined by the sliding mesh technique.

The pressure under-relaxation factor was 0.1, and the momentum under relaxation was 0.28, while other flow parameters of the under-relaxation factor were reduced according to the specific situation. Pressure speed was coupled with Pressure Implicit with Splitting of Operator (PISO), and pressure discrete used Pressure

Table 1
Chemical composition of carbide residue and silica.

	Chemical composition (%)									
	CaO	SiO_2	Al_2O_3	SO_2	MgO	Fe_2O_3	SrO	NaOH	CuO	H_2O
Carbide residue	79.34	3.57	2.14	1.22	0.62	0.21	0.26	–	–	12.64
Silica	0.08	97.46	0.16	1.82	–	0.03	–	0.29	0.02	0.14

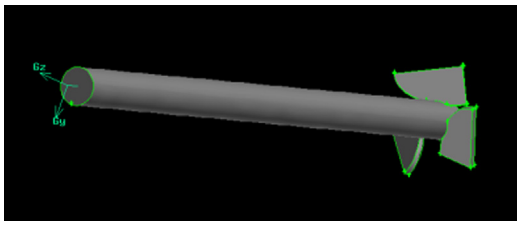

Fig. 1. The component model of stirring paddle.

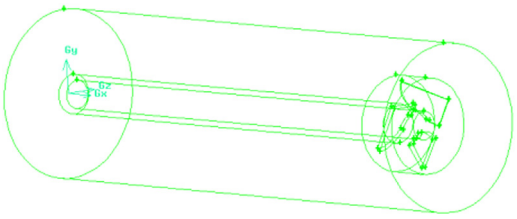

Fig. 2. The computational domain layout of flow field in reactor.

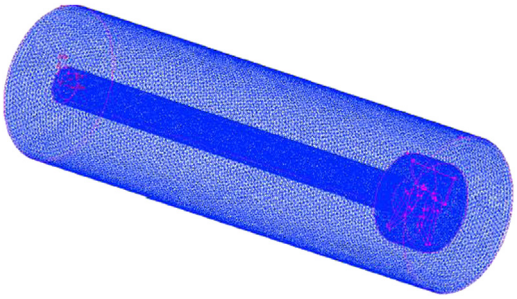

Fig. 3. The partition of computational domain grids.

Staggering Option (PRESTO). The momentum of the discrete adopted the first-order windward scheme initially, followed by the Central Differencing Scheme for iterative computations when the calculations were stabilized.

According to the Neumann stability method, in combination with the existing calculation resources and the accuracy aspect, the unsteady computational time step for the flow close to the 6 h reaction were 0.0016 s, corresponding to the reactor's stirring paddle rotating 1°. The flow stabilized after 8 paddle rotations, after which the parameter value could be identified.

2.4. Solubility experiments

The release of Ca^{2+} and OH^- from CSH was investigated via a series of batch experiments. For each experiment, 1g of CSH was mixed with 1 L of DI water in glass bottles. The bottles were then placed on an agitation table and mixed at 40 rpm at 20 °C for 5, 10, 15, 20, 40, and 60 min. The resulting Ca^{2+} concentration was determined using the EDTA coordination titration method (The relative derivation of data is 0.05%). Solution pH was measured ($\pm$ 0.1) using precise pH paper (San-ai-si Reagent Co. Ltd., Shanghai, China).

2.5. Characterization instruments

The phase component and crystal structure were determined by X-ray diffraction using Cu Kα radiation (XRD, model XD-2 instrument, China). The pore structures were observed by field-emission scanning electron microscopy (FESEM, IUE, Hitachi, Japan), and nitrogen adsorption–desorption isotherms were plotted on a nitrogen adsorption apparatus (BET, ASAP-2010, USA). Particle size distributions were performed with a BT-9300HT laser particle analyzer (0.1 ~ 1000 μm).

3. Results and discussion

3.1. Morphological structure

The FESEM micrographs of all samples indicated that the different stirring speeds resulted in different morphology (Fig. 4). For example, the surface of CSH (30 rpm) was compact and lacked any obvious pore distribution. As the stirring speed increased, these surfaces gradually exhibited a network-like structure. By contrast, the surface of CSH (90 rpm) was a loose reticular structure with massive pore structure distributed on the surface.

3.2. BET surface areas and pore structure

The nitrogen adsorption–desorption isotherms and corresponding pore size distribution curves of the CSH samples are presented in Fig. 5. The isotherm was close to type IV (BDDT classification) with a hysteresis loop at high relative pressure between 0.6 and 1.0, revealing the presence of mesopores (2–50 nm) and macropores (> 50 nm). The shapes of the hysteresis loop were close to type H3, indicating the presence of slit-like pores [28,29] (Fig. 5a). The pore volume, and S_{BET} of CSH increased as the stirring speed increased up to 90 rpm (Table 2), above which (> 110 rpm) no longer increased. The corresponding pore size indicated that the distribution of CSH (30 rpm) ranged from 2 to 100 nm and was bimodal with small mesopores (~3.05 nm), and larger ones (~47.82 nm) (Fig. 5b). The small mesopores and larger ones came from the aggregation of primary particles and secondary particles, respectively. In contrast, the pore size distribution of CSH (90 rpm) was classified into small mesopores (~7.34 nm) range. The smaller mesopores may very well reflect the porosity of CSH samples.

3.3. Particle size distributions

The particle size distribution of CSH samples is presented in Fig. 6. The increase in stirring speed resulted in small particle sizes, and large particle size reflected aggregation during CSH formation. And particle aggregation was the main factor for the preparation of CSH by hydrothermal synthesis method.

3.4. Phase structure

The XRD patterns of as-prepared CSH samples exhibited characteristics reflective of Jennite (PDF card 18-1206, chemical formula $Ca_9Si_6O_{18}(OH)_6{\cdot}8H_2O$) (Fig. 7). According to the fitting of MDI jade5.0, the crystallinity of CSH (30 rpm), CSH (50 rpm), CSH (70 rpm), CSH (90 rpm), and lastly CSH (110 rpm) was

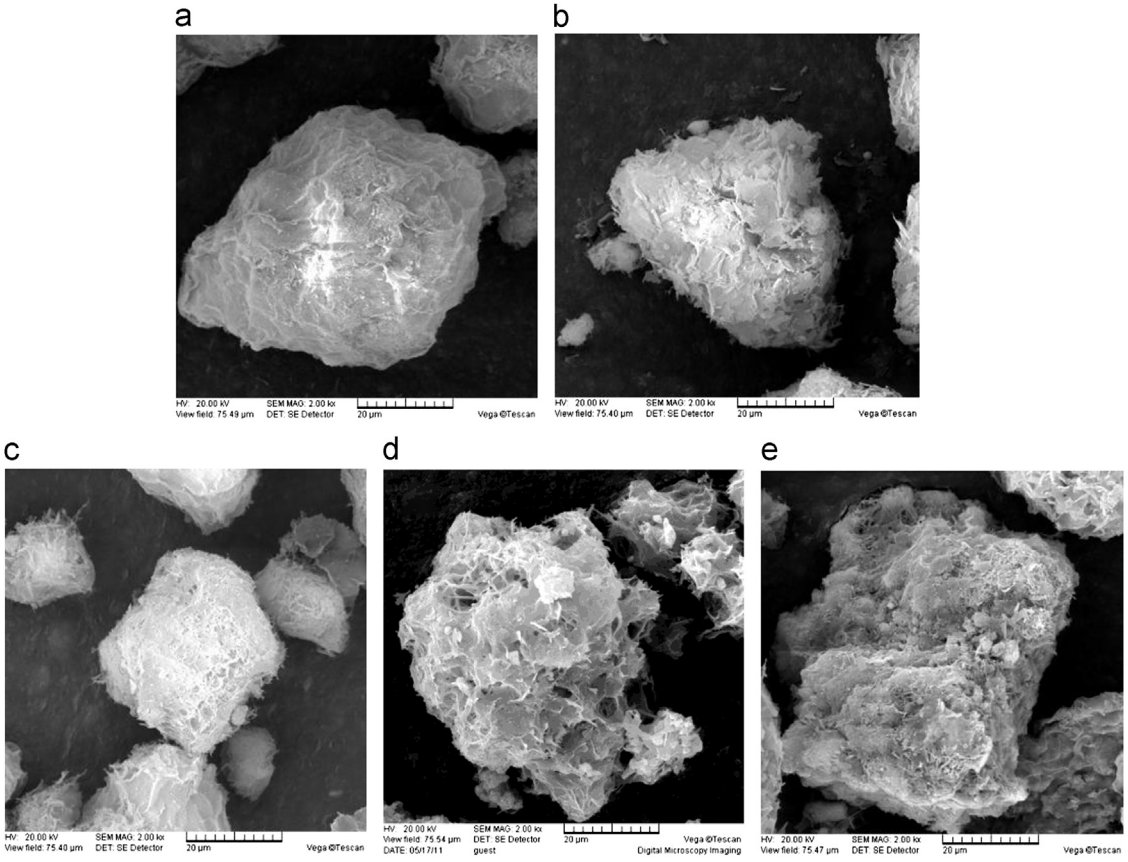

Fig. 4. FESEM images of the CSH (30 rpm) (a), CSH (50 rpm) (b), CSH (70 rpm) (c), CSH (90 rpm) (d) and CSH (110 rpm) (e).

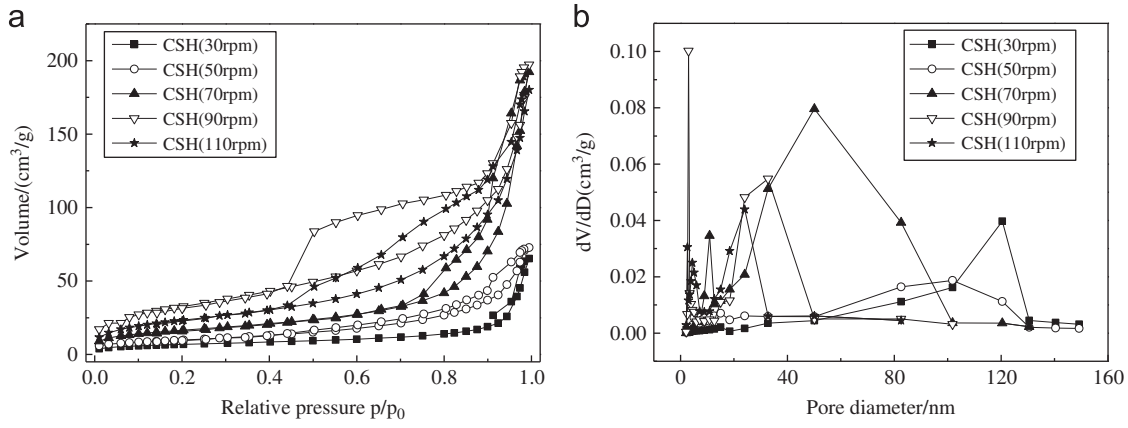

Fig. 5. N_2 adsorption–desorption isotherms (a) and pore-size distribution curves (b) of CSH samples.

Table 2
Specific BET surface areas and pore parameters of CSH samples.

CSH samples	Total volume (cm^3/g)	Peak pore diameter (nm)	S_{BET} (m^2/g)
CSH (30 rpm)	0.10	19.14	25
CSH (50 rpm)	0.11	12.60	35
CSH (70 rpm)	0.28	20.00	60
CSH (90 rpm)	0.31	9.80	120
CSH (110 rpm)	0.30	13.15	86

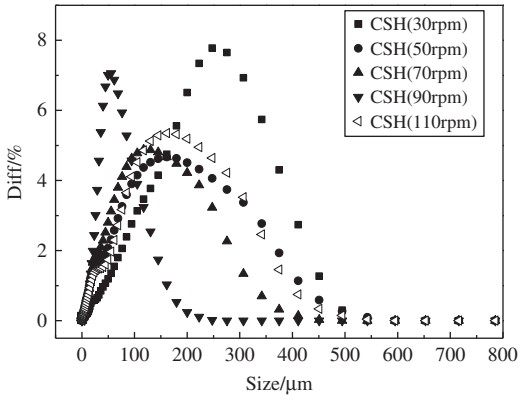

Fig. 6. Particle size distributions of CSH samples.

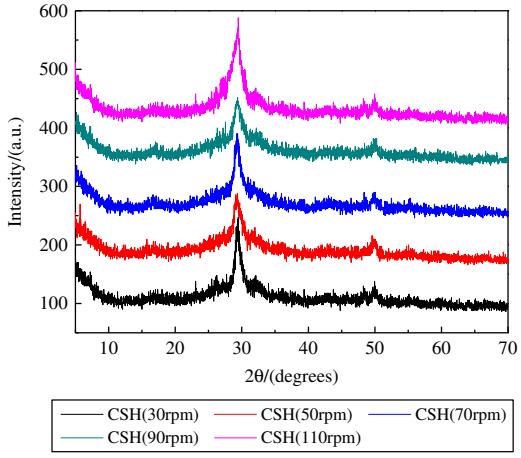

Fig. 7. XRD patterns of CSH samples.

37.46%, 26.53%, 23.17%, 15.75% and 18.03%, respectively. This result indicating that as the stirring speed increased, the main characteristic reflections at $2\theta = 29.92^{\circ}$ of CSH samples gradually decreased and was lowest at 90 rpm. This lowest value was likely related to the lower crystallinity of the sample, suggesting formation of a massive lattice defect, likely a result of the CSH slurry solute adhering to the surface of CSH grains. The density of the CSH slurry also declined as a result of the decreasing solute concentration. Eddies formed in the CSH slurry as a result of shear stress caused by stirring, leading to the inhomogeneous solute concentration on the surface of CSH. Thus, the growth morphology of CSH changed accordingly.

3.5. The formation mechanism of porous structure under the complex flow field condition

3.5.1. The flow field distribution characteristics in the hydrothermal reaction process

The equivalent cloud charts of the vorticity, radial velocity, and axial velocity are presented in Figs. 8a, b and c, respectively. The center of the impeller blades ($X = 181$ mm) was used to analyze the distribution, and changes in shear stress within the reactor cylinder.

The vortices of the polar regions were distributed in three directions (Fig. 8a). This indicated the strong vortex core shear stress turbulence structures influenced each other along the circumferential direction. The shear stress that changed periodically along the circumference had a greater effect on the outer or inner area along the radial region. The vortex core decay energy spread primarily outward in a radial direction. And the attenuation rate gradually reduced outward along this radial.

The area of the outer radial velocity component was the maximum concentrates in the root of impeller blade (Fig. 8b). The area of the inner radial velocity component was the maximum concentrates in the tip of impeller blade and the area of inner surface in reaction tube. The radial shear stress effects in aforementioned areas were large. And the energy distribution was more average than axial shear stress effect, and had more obvious characteristics in the transmission of radial shear stress effects.

The region where the axial velocity component was comparatively large was mainly distributed between the root and the leaf areas of the impeller blade (Fig. 8c). These areas also exhibited a strong axial shear stress effect. The combination of these effects resulted in the formation of an orthogonal shear force field distribution, indicating that energy transmission of the flow field shear had strong directional characteristics.

3.5.2. The formation process of porous structure

The combination of flow field distribution features during the hydrothermal reaction allowed for elucidation of the CSH porous structure formation mechanism. The formation process of CSH was in progress during a complex phase condition; however, CSH with porous structure could be obtained effectively under a reasonable stirring speed (90 rpm). Initially as the pressure within the reaction kettle increased, the Si–O bond within SiO_2 was broken and the degrees of freedom of the silicon oxygen tetrahedron increased, resulting in the formation of $H_3SiO_4^-$ as indicated in the reactions series (1–2) below

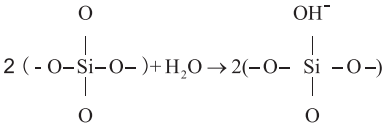

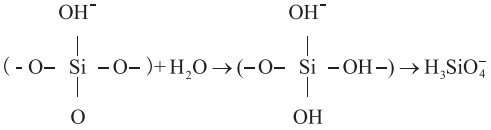

Simultaneously, CaO reacted with water to generate $Ca(OH)_2$. This $Ca(OH)_2$ then ionized to Ca^{2+} and OH^-, both then reacting with $H_3SiO_4^-$ to form a CSH gel as indicated by the below (3).

$$4OH + 2H_3SiO_4^- + 3Ca^{2+} \rightarrow 3CaO_2SiO_2 \cdot 3H_2O \rightarrow C-S-H + 2H_2O \quad (3)$$

Therefore, the formation of forming CSH was in fact a phase transformation process. According to thermodynamic theory,

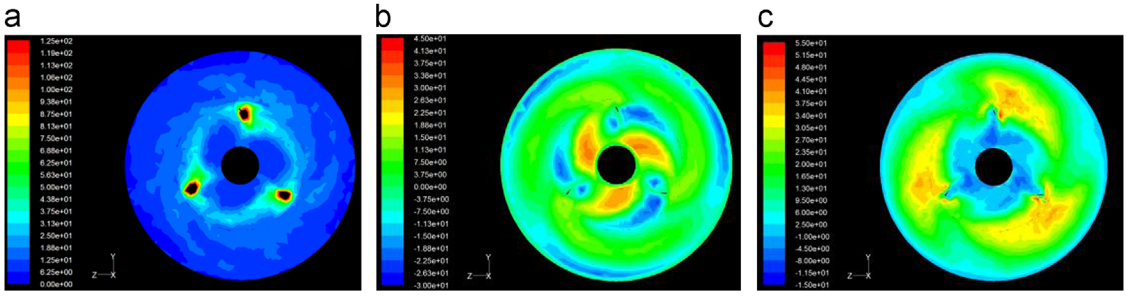

Fig. 8. The distribution and changes of the shear stress in the cylinder of the reactor. (a) The equivalent cloud charts of the vorticity (X=181 mm); (b) the equivalent cloud charts of radial velocity (X=181 mm); (c) the equivalent cloud charts of axial velocity (X=181 mm).

phase transformation can occur spontaneously only when a system has reached a supersaturation critical value [15]. Thus, the production speed of CSH also depends on supersaturation on the surface of the particles. Further increasing saturation may very likely result in greater CSH production, but also break the stable growth of the particle to form the porosity of CSH. The vorticity distribution of the CSH slurry, (due to the sheer force produced by stirring), indicated an obvious concentration gradient in the area extending outward along the surface of CSH particles. The concentration of Ca^{2+}, OH^-, and $H_3SiO_4^-$ near the surface of the particles was the largest, and this concentration gradually decreased extending outward of this area.

It is worthy to note that when the stirring intensity was too low, the viscosity near the surface of particles was so high that it forced particles to reunite during the CSH formation process. This resulted in a dense CSH surface structure. Conversely when the stirring intensity was too high the highly concentrated supersaturation state near the CSH surface could not form. This resulted in a decreased nucleation rate, subsequently affecting CSH.

3.6. The solubility and dissolution kinetics of CSH

The Ca^{2+} released, and the changes of pH are presented in Fig. 9a and b, respectively. Comparatively, the CSH samples prepared at a high stirring speed exhibited better Ca^{2+} and OH^- dissolution properties.

The dissolution rate equation of CSH obtained under different stirring speeds is as follows (4–8):

$$\frac{dX_t}{dt} = k(T)f(X_t)f(t) \tag{4}$$

$$f(X_t) = (1-X_t)^m \tag{5}$$

$$f(t) = t^n \tag{6}$$

$$k(T) = k_0 e^{\frac{-E}{RT}} \tag{7}$$

Substituting Eqs. (5), (6) and (7) into Eq. (4), respectively, to obtain the following equation:

$$\frac{dX_t}{dt} = k_0 e^{\frac{-E}{RT}}(1-X_t)^m t^{n_a} \tag{8}$$

where n_a is the time index of dissolution, which reflected the relationship between dissolution and time. This was the reaction relation in the most of the models; m is the concentration index of dissolution, which reflected the relationship between dissolution rate and crystallinity; E is the activation energy; R is the gas constant; T is the absolute temperature. Boundary conditions of Eq. (8) was $t=0$, $X_0=0$; $T=\infty$, $X_\infty=1$. During the dissolving process, k_a is a constant. Therefore, Eq. (8) can be expressed as follows:

$$\frac{dX_t}{dt} = k_a(1-X_t)^m t^{n_a} \tag{9}$$

When $m=1$, Eq. (9) can be transformed as follows:

$$\frac{dX_t}{(1-X_t)} = k_a t^n dt \tag{10}$$

Integrating Eq. (10), and then taking the logarithm of both sides, results in Eq. (11)

$$\ln[-\ln(1-X_t)] = (n+1)\ln t + \ln\frac{k_a}{n+1} \tag{11}$$

Eq. (11) can then be transformed into the classical Avrami equation [30]:

$$-\ln(1-x) = kt^n \tag{12}$$

where k is the rate constant; n is the solubility index, which is related to the characteristics of the solid phase; t is the reaction time. X_t is the solution fraction (It is equal to the ratio C_t/C_{max}, C_t is the concentration at the reaction time of t; C_{max} is the maximum solution concentration). By fitting $-\ln(1-x)$ *vt.* t^n, the dissolution rule of various materials can be described by Avrami dynamics model (Fig. 10). In addition, the dissolution rate constant k of the CSH sample was positively correlated with its S_{BET}, and negative correlated with its particle size and crystallinity. This suggests that k is related to the S_{BET} (S), the particle diameter (I) and the crystallinity (D) of the material. Therefore, the expression among k, S, I and D can be deduced as follows:

$$k = k_0 S^a I^b D^c \tag{13}$$

where k_0, a, b and c were constants and can be fitted to be k_0=0.7643, a=0.5962, b=–0.7835, c=–0.4413, respectively. Thus, Eq. (13) could be expressed as follows:

$$k = 0.7643 S^{0.5962} I^{(-0.7835)} D^{(-0.4413)} \tag{14}$$

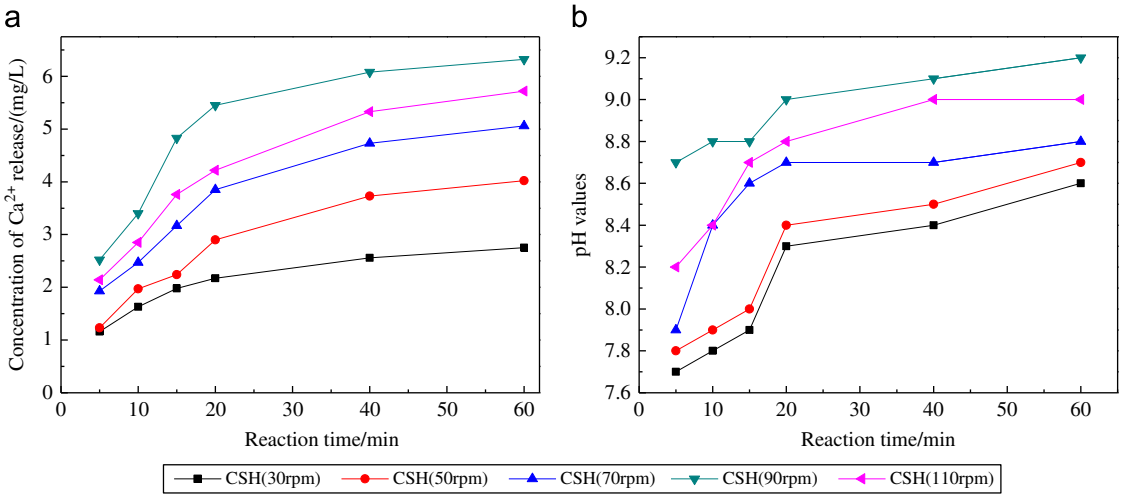

Fig. 9. Concentration of Ca^{2+} released from CSH samples (a) and pH in deionized water kept by CSH samples (b).

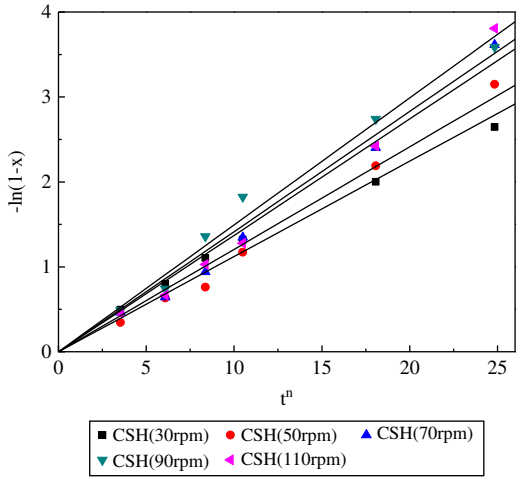

Fig. 10. Variation of $-\ln(1-x)$ versus t^n for CSH samples.

The relationship between S, I, D and concentration of Ca^{2+} released can be deduced by substituting Eq. (14) into Eq. (12)

$$-\ln(1-x) = 0.7643 S^{0.5962} I^{(-0.7835)} D^{(-0.4413)} t^{0.7846} \quad (15)$$

According to Eq. (15), the small particle size and low crystallinity and large S_{BET} played a key role in enhancing the capacity of Ca^{2+} and OH^- release of CSH.

4. Conclusions

Porous CSH was synthesized hydrothermally under different stirring speeds. The complex fluid flow during the formation process was revealed via use of the Improved of Detached Eddy Simulation (IDDES) as the turbulence model. Under a proper stirring speed (90 rpm), the as-prepared CSH (with large surface areas and pore volume, small particle size and low crystallinity), released greater quantities of Ca^{2+} and OH^-. This study presents an effective approach to determining the CSH formation mechanism under complex phase conditions. These data are essential for use in furthering our understanding of the existing limitations of CSH use as a P removal and recycling method.

References

[1] H. Maeda, E.H. Ishida, Hydrothermal preparation of diatomaceous earth combined with calcium silicate hydrate gels, Journal of Hazardous Materials 185 (2011) 858–861.
[2] K. Okano, M. Uemoto, J. Kagami, K. Miura, T. Aketo, M. Toda, K. Honda, H. Ohtake, Novel technique for phosphorus recovery from aqueous solutions using amorphous calcium silicate hydrates (A-CSHs), Water Research 47 (2013) 2251–2259.
[3] X.C. Chen, H.N. Kong, D.Y. Wu, X.Z. Wang, Y.Y. Lin, Phosphate removal and recovery through crystallization of hydroxyapatite using xonotlite as seed crystal, Journal of Environmental Sciences 21 (2009) 575–580.
[4] A. Renman, G. Renman, Long-term phosphate removal by the calcium-silicate material Polonite in wastewater filtration systems, Chemosphere 79 (2010) 659–664.
[5] W. Guan, F.Y. Ji, Q.K. Chen, P. Yan, Q. Zhang, Preparation and phosphorus recovery performance of porous calcium-silicate-hydrate, Ceramics International 39 (2013) 1385–1391.
[6] D. Seyhan, Country-scale phosphorus balancing as a base for resources conservation, Resources, Conservation and Recycling 53 (2009) 698–709.
[7] C.J. Dawson, J. Hilton, Fertilizer availability in a resource-limited world: production and recycling of nitrogen and phosphorus, Food Policy 36 (2011) S14–S22.
[8] D. Cordell, J.O. Drangert, S. White, The story of phosphorus: global food security and food for thought, Global Environmental Change 19 (2009) 292–305.
[9] H. Kodera, M. Hatamoto, K. Abe, T. Kindaichi, N. Ozaki, A. Ohashi, Phosphate recovery as concentrated solution from treated wastewater by a PAO-enriched biofilm reactor, Water Research 47 (2013) 2025–2032.
[10] N. Martí, L. Pastor, A. Bouzas, J. Ferrer, A. Seco, Phosphorus recovery by struvite crystallization in WWTPs: influence of the sludge treatment line operation, Water Research 44 (2010) 2371–2379.
[11] Z. Bradford-Hartke, P. Lant, G. Leslie, Phosphorus recovery from centralized municipal water recycling plants, Chemical Engineering Research and Design 90 (2012) 78–85.
[12] J.C. Jeffrey, J.T. Jeffrey, F.W.T. Hal, M.J. Hamlin, Solubility and structure of calcium silicate hydrate, Cement and Concrete Research 34 (2004) 1499–1519.
[13] P. Ptáček, M. Nosková, J. Brandštetr, F. Šoukal, T. Opravil, Mechanism and kinetics of wollastonite fibre dissolution in the aqueous solution of acetic acid, Powder Technology 206 (2011) 338–344.

[14] I. Baur, P. Keller, D. Mavrocordatos, B. Wehrli, C.A. Johnson, Dissolution–precipitation behaviour of ettringite, monosulfate, and calcium silicate hydrate, Cement and Concrete Research 34 (2004) 341–348.
[15] D. Sugiyama, T. Fujita, A thermodynamic model of dissolution and precipitation of calcium silicate hydrates, Cement and Concrete Research 36 (2006) 227–237.
[16] S. Shaw, S.M. Clark a,b, C.M.B. Henderson, Hydrothermal formation of the calcium silicate hydrates, tobermorite ($Ca_5Si_6O_{16}(OH)_2.4H_2O$) and xonotlite ($Ca_6Si_6O_{17}(OH)_2$): an in situ synchrotron study, Chemical Geology 167 (2000) 129–140.
[17] M.M. Amini, M. Mirzaee, Effect of solvent and temperature on the preparation of potassium niobate by hydrothermal-assisted sol-gel processing, Ceramic International 35 (2009) 2367–2372.
[18] M. Özen, M. Mertens, J. Luyten, F. Snijkers, H. D'Hondt, P. Cool, Hydrothermal synthesis of carbonate-free submicron-sized barium titanate from an amorphous precursor: Synthesis and characterization, Ceramic International 38 (2012) 619–625.
[19] S. Murakami, K. Kato, Y. Enari, M. Kamitakahara, N. Watanabe, K. Ioku, Hydrothermal synthesis of porous hydroxyapatite ceramics composed of rod-shaped particles and evaluation of their fracture behavior, Ceramic International 38 (2012) 1649–1654.
[20] M.A.S. Anjos, A.E. Martinelli, D.M.A. Melo, Effect of sugarcane biomass waste in cement slurries submitted to high temperature and pressure, Materials Science and Engineering A 529 (2011) 49–54.
[21] J. Kikuma, M. Tsunashima, T. Ishikawa, S. Matsuno, A. Ogawa, K. Matsui, M. Sato, Journal of Solid State Chemistry 184 (2011) 2066–2074.
[22] H. Youssef, D. Ibrahim, S. Komarneni, K.J.D. Mackenzie, Synthesis of 11 Å Al-substituted tobermorite from trachyte rock by hydrothermal treatment, Ceramic International 36 (2010) 203–209.
[23] X.L. Zhao, S. Masaihiko, Fractionation and solubility of cadmium in paddy soils amended with porous hydrated calcium silicate, Journal of Environmental Sciences 19 (2007) 343–347.
[24] Luc Nicoleau, Accelerated growth of calcium silicate hydrates: experiments and simulations, Cement and Concrete Research 41 (2011) 1339–1348.
[25] M.Q. Li, H.X. Liang, Formation of micro-porous spherical particles of calcium silicate (xonotlite) in dynamic hydrothermal process, China Particuology 2 (2004) 124–127.
[26] P.D. Suresh, V. Kumar, R. Sripriya, S. Chakraborty, B.C. Meikap, Performance characteristics of pilot plant dense media hydro-cyclone, Chemical Engineering Science 65 (2010) 4661–4671.
[27] W.C. Yan, D.P. Shi, Z.H. Luo, Y.H. Lu, Three-dimensional CFD study of liquid–solid flow behaviors in tubular loop polymerization reactors: the effect of guide vane, Chemical Engineering Science 66 (2011) 4127–4137.
[28] F. Dong, Y.J. Sun, M. Fu, Z.B. Wu, S.C. Lee, Room temperature synthesis and highly enhanced visible light photocatalytic activity of porous BiOI/BiOCl composites nanoplates microflowers, Journal of Hazardous Materials 219–220 (2012) 26–34.
[29] F. Dong, Y.J. Sun, M. Fu, W.K. Ho, S.C. Lee, Z.B. Wu, Novel in situ n-doped $(BiO)_2CO_3$ hierarchical microspheres self-assembled by nnosheets as efficient and durable visible light driven photocatalyst, Langmuir 28 (2012) 766–773.
[30] F.A. Celik, S. Kazanc, Crystallization analysis and determination of Avrami exponents of CuAlNi alloy by molecular dynamics simulation, Physica B 409 (2013) 63–70.